Electronic Supplementary Material (ESI) for Nanoscale.

Supplementary Information

Anisotropic mechanical properties of α-MoO_3 nanosheets

Congying Wang[a,b], Xuwei Cui[a,c], Shijun Wang[a], Wenlong Dong[a,b], Hai Hu[d], Xiaoyong Cai[d], Chao Jiang[d], Zhong Zhang[c,*] and Luqi Liu,[a,b,*]

[a] CAS Key Laboratory of Nanosystem and Hierarchical Fabrication and CAS Center for Excellence in Nanoscience, National Center for Nanoscience and Technology, Beijing, 100190, China.

[b] University of Chinese Academy of Sciences, Beijing, 100049, China.

[c] CAS Key Laboratory Mechanical Behavior and Design of Materials, Department of Modern Mechanics, University of Science and Technology of China, Hefei, 230027, China.

[d] CAS Key Laboratory of Standardization and Measurement for Nanotechnology and CAS Center for Excellence in Nanoscience, National Center for Nanoscience and Technology, 100190 Beijing, China.

* Corresponding author.

*Address correspondence to Email:

liulq@nanoctr.cn; zhangzhong@ustc.edu.cn

Section S1. Raman characterization for anisotropic structure of α-MoO_3.

The lattice orientations of α-MoO_3 nanosheets were identified through angle resolved polarized Raman spectroscopy (633nm laser) with 10° step. The laser and analyzer are set in parallel configuration and the laboratory coordinate and crystal coordinate are coincident (Fig. S1a). Here, we specify the angle between the direction of incident light and a-axis as θ.

For α-MoO_3, four of its lattice vibrational modes are Raman active, including A_g, B_{1g}, B_{2g}, and B_{3g}. We only focus on A_g and B_{2g} modes. The intensity of a given Raman mode is a function of Raman tensor and scattering geometry,

$$I \propto |e_i \cdot R \cdot e_s|^2 \tag{S1}$$

where R is Raman tensor, e_i and e_s are the unit vector of incident laser polarization and the scattering phonon polarization, respectively. Here the Raman tensor can be written as

$$R(A_g) = \begin{pmatrix} A & 0 & 0 \\ 0 & B & 0 \\ 0 & 0 & C \end{pmatrix} \tag{S2}$$

$$R(B_{2g}) = \begin{pmatrix} 0 & 0 & E \\ 0 & 0 & 0 \\ E & 0 & 0 \end{pmatrix} \tag{S3}$$

The e_i is parallel to e_s, and they can be written as $e_i = {e_s}^T = (1 \quad 0 \quad 0)$. Because the Raman tensors (R) of a crystal are defined according to its crystal coordinates, it must be converted into laboratory coordinates (R') by $R' = MRM^T$, M is defined as a transform matrix，

$$\begin{pmatrix} x \\ y \\ z \end{pmatrix} = M \begin{pmatrix} a \\ b \\ c \end{pmatrix} \tag{S4}$$

$$M = \begin{pmatrix} \cos\theta & 0 & -\sin\theta \\ 0 & 1 & 0 \\ \sin\theta & 0 & \cos\theta \end{pmatrix} \tag{S5}$$

Back substituting into Eq. (S1), the Raman intensity is given by

$$I \propto |e_i \cdot M \cdot R \cdot M^T \cdot e_s|^2 \tag{S6}$$

According to Eq. (S2), Eq. (S3) and Eq. (S6), the intensity of the peaks of two vibrational modes with Raman activity can be expressed by the following Eq S7,

$$I(A_g) \propto (A\cos^2\ \theta + C\sin^2\ \theta)^2 \quad \text{(S7)}$$

$$I(B_{2g}) \propto E^2\sin^2\ 2\theta \quad \text{(S8)}$$

Fig. 1g, h and Fig. S1b, c present the normalized Raman intensity in the polar representation and theoretical fitting curve according to above description. The intensity period of A_g mode is 180° and B_{2g} is 90°. Apparently, the theoretical calculation is in good agreement with the experimental results.

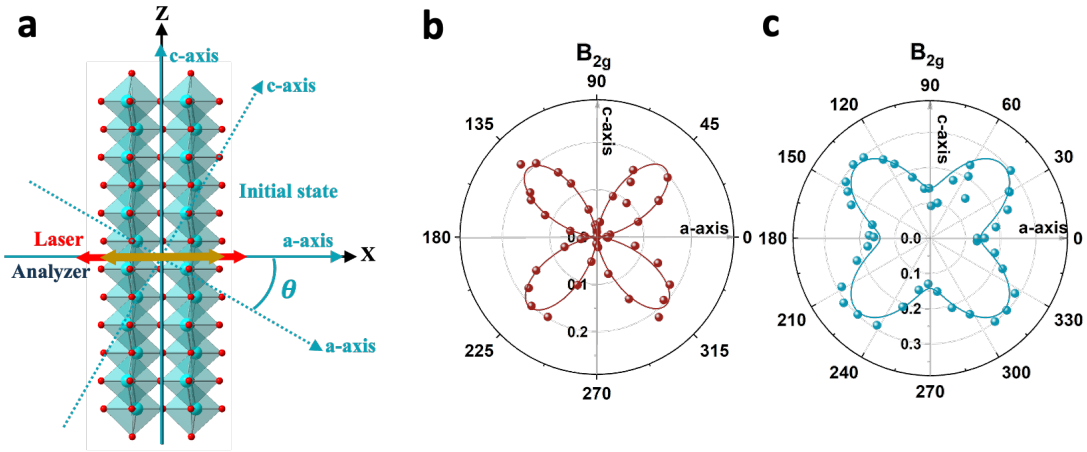

Fig. S1 (a) Structure diagram of angle resolved polarized Raman experiment, black arrows (xz) indicate the laboratory coordinate; green arrows (ac) stand for the crystal coordinate; red arrow represents the incident laser polarization direction; yellow arrow indicates the analyzer direction. (b) Theoretical (solid lines) and experimental (circles) profiles of angle-resolved normalized intensities of Raman B_{2g} (115 cm^{-1}) and B_{2g} (283 cm^{-1}) modes.

Section S2. The calculation of surface free-energy.

The contact angle is typically measured at the cross-point where a liquid-vapor interface interacts with a solid surface (schematic Fig. S2). The results for the contact angles of different liquids (diiodomethane (DM), water (H_2O), ethanol (EtOH) and isopropanol (IPA)) on SiO_2/Si and MoO_3 substrates are summarized in Table S1. In general, the wettability of a solid surface by a liquid can be defined by Young-Dupré equation (Eq. S9),

$$\gamma_{s-l} = \gamma_s - \gamma_l \cos\theta_s \quad \text{(S9)}$$

where, γ_{s-l} is the free energy between the substrate and liquid, γ_s is the surface free energy of the substrate, γ_l is the free energy of liquid. θ_s is the contact angle between substrate and liquid. Here, the substrates include SiO_2/Si and MoO_3, liquids include DM, H_2O, EtOH and IPA.

In the past several decades, some semi-empirical analytical models have been developed to estimate the surface free energy derived from the contact angles.[1] According to Owens and Wendt model, the surface energy of solids consisted of dispersion and dipole-hydrogen bonding forces.[1] In order to extract the solid-liquid interfacial free energy (γ_{s-l}) and the solid surface free energy (γ_s), at least two liquids with known dispersive and polar components of surface tensions are required. Here, H_2O and DM with well-known polar γ_l^{p} and dispersion γ_l^{d} components were used to derive γ_s and γ_{s-l} as presented by the following equations:

$$\gamma_l = \gamma_l^P + \gamma_l^d \quad \text{(S10)}$$

$$\gamma_s = \gamma_s^P + \gamma_s^d \quad \text{(S11)}$$

$$\gamma_{s-l} = \gamma_s + \gamma_l - 2\left(\sqrt{\gamma_s^d \gamma_l^{\mathrm{d}}} + \sqrt{\gamma_s^P \gamma_l^{\mathrm{p}}}\right) \quad \text{(S12)}$$

where γ_s^P and γ_l^{p} are polar components, γ_s^d and γ_l^{d} are dispersive components of substrate and liquid surface energies, respectively. Based on the measured contacting angles, θ, the polar γ_s^P and dispersion γ_s^d components were calculated using Eq. (S13), as derived from Eq. (S9) and Eq. (S12):

$$\gamma_l(1 + \cos\theta) = 2\left(\sqrt{\gamma_s^d \gamma_l^{\mathrm{d}}} + \sqrt{\gamma_s^P \gamma_l^{\mathrm{p}}}\right) \quad \text{(S13)}$$

Table S2 shows the measured surface energies of SiO_2/ Si and MoO_3. Then, we could calculate $\gamma_{SiO_2-MoO_3}$ based on the Eq S14 derived from Young-Dupré equation and Owens-Wendt model[1] to:

$$\gamma_{SiO_2-MoO_3} = (\sqrt{\gamma^d_{SiO_2}} - \sqrt{\gamma^d_{MoO_3}})^2 + (\sqrt{\gamma^p_{SiO_2}} - \sqrt{\gamma^p_{MoO_3}})^2 \quad \text{(S14)}$$

Consequently, the calculated value of $\gamma_{SiO_2-MoO_3}$ is 0.44 mJ/m^2.

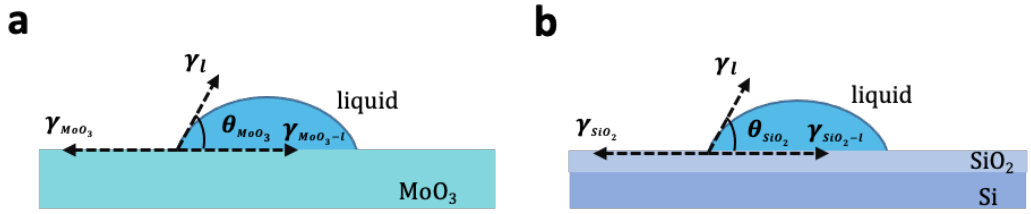

Fig. S2 Schematic showing surface tension equilibrium of a liquid droplet on (a) MoO_3 and (b) SiO_2 surface.

Table S1. Contact angle of SiO_2/Si and MoO_3 with different liquids.

Substrate	Contact angle [deg]			
	DM	H_2O	EtOH	IPA
SiO_2	32.7 ± 0.6	30.0 ± 1.0	0	0
MoO_3	31.0	26.0	31.0	20.5

Table S2. Surface free energy of SiO_2/Si, MoO_3, DM and H_2O.

Surface energy (mJ/m^2)	SiO_2	MoO_3	DM[1]	H_2O[1]
γ^d	32.6	27.5	49.5	21.8
γ^p	33.4	39.0	1.3	51.0
$\gamma = \gamma^d + \gamma^p$	66.0 (γ_{SiO_2})	66.5 (γ_{MoO_3})	50.8 (γ_{DM})	72.8 (γ_{H_2O})

Section S3. The contact angle measurement.

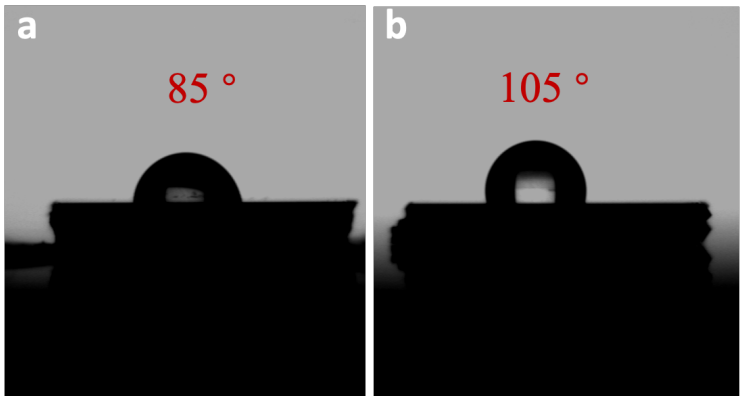

Fig. S3 Contact angles of water on the surface of PTP device: (a) with plasma treatment and (b) without.

Section S4. Transfer process of MoO_3.

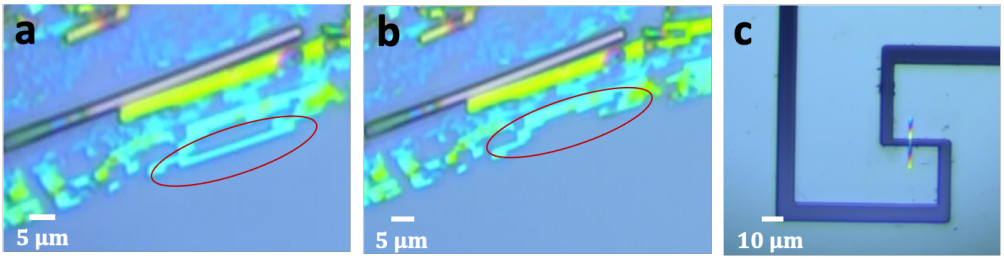

Fig. S4 (a, b) Optical images of MoO_3 nanosheets exfoliated onto SiO_2/Si substrate. Red circle indicated the MoO_3 before (a) and after transfer (b). (c) MoO_3 nanosheet deposited onto PTP surface.

Section S5. Thickness measurement of MoO_3.

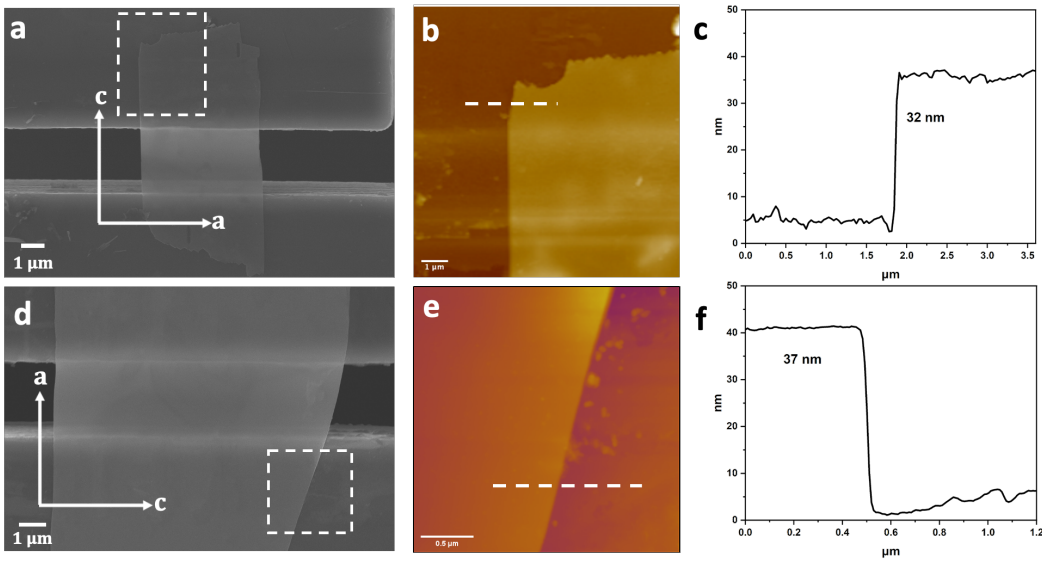

Fig. S5 (a, b) SEM images along c-axis and along a-axis. (b, e) AFM images of MoO_3 for the marked area in (a, b). (c, f) Corresponding height profiles of MoO_3 along dash line.

Section S6. SEM images of the tested specimens.

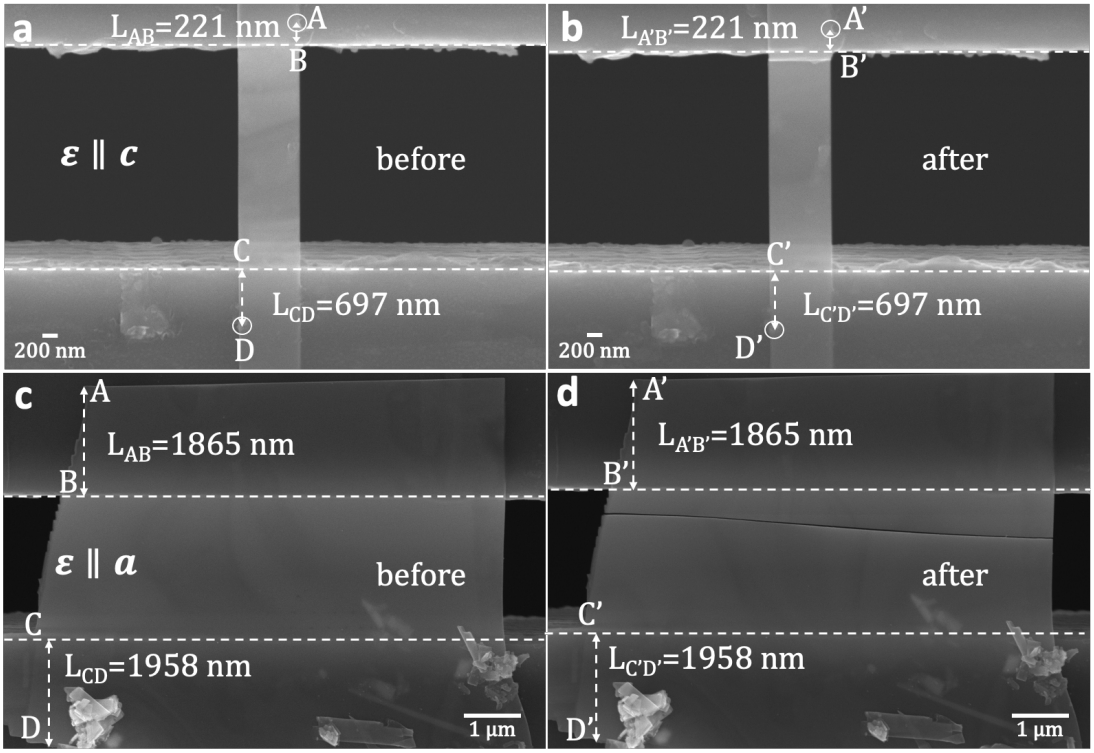

Fig. S6 The SEM images of MoO_3 nanosheets before and after tensile tests (a, b) along c-axis and (c, d) along a-axis. The measured distance: L_{AB}=$L_{A'B'}$= 221 nm, L_{CD}=$L_{C'D'}$=697 nm along c-axis, L_{AB}=$L_{A'B'}$=1865 nm, L_{CD}=$L_{C'D'}$=1958 nm along a-axis.

Section S7. Anisotropy ratio of Young's modulus of various anisotropic 2D materials.

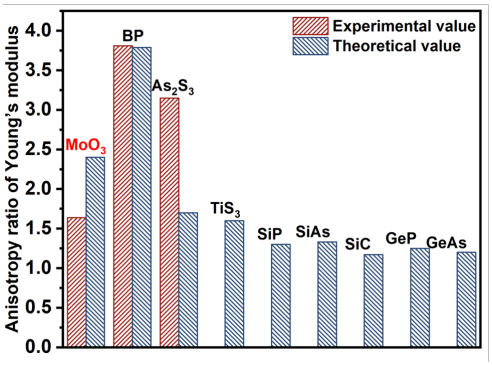

Fig. S7 Summary of in-plane anisotropy ratio of Young's modulus of various anisotropic 2D materials (MoO_3[2], BP,[3] As_2S_3,[4,5] TiS_3,[6] SiP,[7] SiAs,[7] SiC,[8] GeP[7] and GeAs[7]).

Section S8. Size effect of fracture strength.

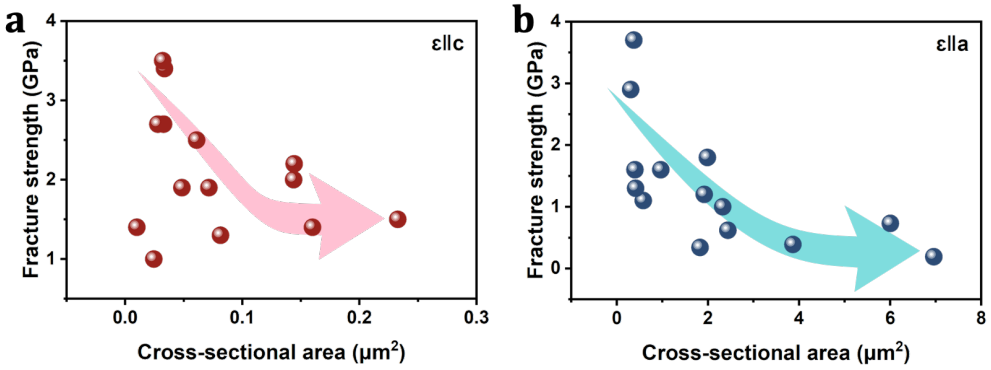

Fig. S8 Fracture strength of MoO_3 nanosheets as a function of cross-sectional area: (a) along c-axis and (b) along a-axis. The arrows are plotted to guide the eye.

Section S9. Characterization of FIB-Cut MoO_3 before and after tensile test.

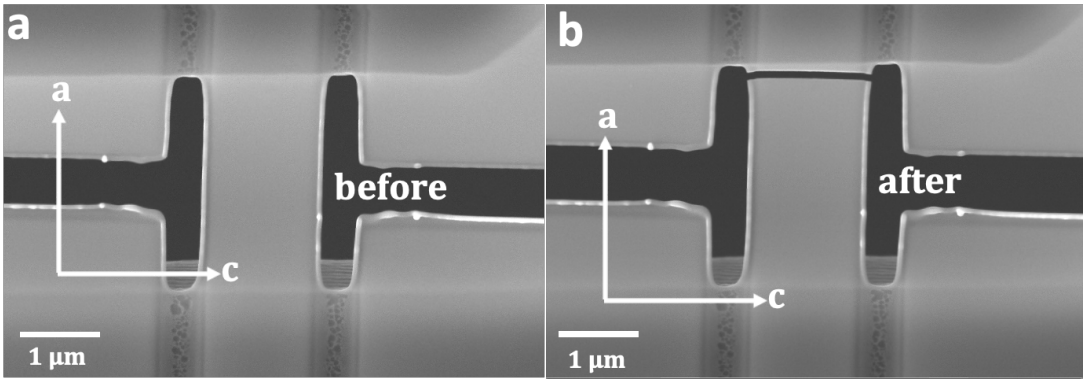

Fig. S9 (a, b) SEM images of MoO_3 trimmed by FIB before and after fracture along a-axis.

Table S3. Geometry and mechanical properties of MoO_3.

Sample	Width (μm)	Thickness (nm)	Young' s modulus (GPa)	Fracture strength (GPa)	Fracture Strain (%)
$\varepsilon \parallel c-1$	5.0	32	96.4	1.4	1.4
$\varepsilon \parallel c-2$	0.3	33	75.5	1.4	1.8
$\varepsilon \parallel c-3$	0.8	41	84.4	2.7	3.3
$\varepsilon \parallel c-4$	0.8	41	119.0	3.5	2.8
$\varepsilon \parallel c-5$	0.6	44	89.8	2.7	3.2
$\varepsilon \parallel c-6$	0.5	49	85.2	1.0	1.9
$\varepsilon \parallel c-7$	0.6	56	105.5	3.4	2.9
$\varepsilon \parallel c-8$	1.0	61	103.9	2.5	2.3
$\varepsilon \parallel c-9$	0.8	64	78	1.9	2.5
$\varepsilon \parallel c-10$	1.1	74	56.8	1.3	2.0
$\varepsilon \parallel c-11$	2.0	74	59.6	2.2	3.7
$\varepsilon \parallel c-12$	1.6	88	60.1	2.0	3.3
$\varepsilon \parallel c-13$	2.3	103	62.9	1.5	2.1
$\varepsilon \parallel c-14$	0.5	143	64.7	1.9	2.9
$\varepsilon \parallel a-1$	8.5	36	53.3	0.9	2.9
$\varepsilon \parallel a-2$	10.1	37	61.2	1.4	3.7
$\varepsilon \parallel a-3$	14.9	39	66.2	0.4	1.1
$\varepsilon \parallel a-4$	9.4	44	57.6	0.6	1.3
$\varepsilon \parallel a-5$	8.0	50	41.0	0.6	1.6
$\varepsilon \parallel a-6$	10.0	105	61.2	1.4	2.2
$\varepsilon \parallel a-7$	15.5	150	35.2	1.0	2.9
$\varepsilon \parallel a-8$	10.5	174	22.8	0.3	1.2
$\varepsilon \parallel a-9$	12.2	200	22.8	0.6	2.6
$\varepsilon \parallel a-10$	9.8	203	40.3	1.8	4.0

$\varepsilon \parallel a-11$	18.5	209	48.4	0.4	0.8
$\varepsilon \parallel a-12$	9.8	203	40.3	1.8	4.0
$\varepsilon \parallel a-13$	18.5	209	48.4	0.4	0.8
$\varepsilon \parallel a-14$	14	404	14.3	0.8	2.6
$\varepsilon \parallel a-1$ (FIB)	1.6	96	44.7	0.7	1.2

Supplementary Video S1. Fracture of α-MoO_3 under *in situ* SEM tensile loading.

References

1. D. K. Owens and R. C. Wendt, *J. Appl. Polymer. Sci.*, 1969, **13**, 1741-1747.

2. S. Puebla, R. D'Agosta, G. Sanchez-Santolino, R. Frisenda, C. Munuera and A. Castellanos-Gomez, *NPJ 2D Mater. and Appl.*, 2021, **5**, 37.

3. X. Cui, W. Dong, S. Feng, G. Wang, C. Wang, S. Wang, Y. Zhou, X. Qiu, L. Liu, Z. Xu and Z. Zhang, *Small*, 2023, **19**, 202301959.

4. M. Siskins, M. Lee, F. Alijani, M. R. van Blankenstein, D. Davidovikj, H. S. J. van der Zant and P. G. Steeneken, *ACS Nano*, 2019, **13**, 10845-10851.

5. M. Dong, Y. Sun, D. J. Dunstan and D. G. Papageorgiou, *Nanoscale*, 2022, **14**, 7872-7880.

6. J. Zhang, X. Liu, Y. Wen, L. Shi, R. Chen, H. Liu and B. Shan, *ACS Appl. Mater. Inter.*, 2017, **9**, 2509-2515.

7. B. Mortazavi and T. Rabczuk, *Physica E. Low. Dimens. Syst. and Nanost.*, 2018, **103**, 273-278.

8. A. S. M. J. Islam, M. S. Islam, N. Ferdous, J. Park, A. G. Bhuiyan and A. Hashimoto, *Mater. Res. Express*, 2019, **6**, 125073.